



HAL
open science

Diffuse-interface modelling of multicomponent diffusion and phase separation in the U-O-Zr ternary system

Mirantsoa-Aimé Rasolofomanana, Clément Cardon, Mathis Plapp, Thomas Philippe, Hervé Henry, Romain Le Tellier

► **To cite this version:**

Mirantsoa-Aimé Rasolofomanana, Clément Cardon, Mathis Plapp, Thomas Philippe, Hervé Henry, et al.. Diffuse-interface modelling of multicomponent diffusion and phase separation in the U-O-Zr ternary system. Computational Materials Science, 2022, 214, pp.111650. 10.1016/j.commatsci.2022.111650 . cea-04017202

HAL Id: cea-04017202

<https://cea.hal.science/cea-04017202v1>

Submitted on 7 Mar 2023

HAL is a multi-disciplinary open access archive for the deposit and dissemination of scientific research documents, whether they are published or not. The documents may come from teaching and research institutions in France or abroad, or from public or private research centers.

L'archive ouverte pluridisciplinaire **HAL**, est destinée au dépôt et à la diffusion de documents scientifiques de niveau recherche, publiés ou non, émanant des établissements d'enseignement et de recherche français ou étrangers, des laboratoires publics ou privés.

Diffuse-interface modelling of multicomponent diffusion and phase separation in the U-O-Zr ternary system

M.A. Rasolofomanana^{a,b,*}, C. Cardon^{a,b}, M. Plapp^b, T. Philippe^b, H. Henry^b, R. Le Tellier^a

^aCEA, DES, IRESNE, DTN, Cadarache
F-13108 Saint Paul-lez-Durance, France

^bLaboratoire de Physique de la Matière Condensée, Ecole Polytechnique
F-91128 Palaiseau, France

Abstract

The ternary mixture of uranium, zirconium and oxygen is investigated as a minimal model for corium, the mixture that forms after the meltdown of a nuclear reactor. Like corium, U-O-Zr exhibits a liquid-liquid phase separation between a metal-rich and an oxide-rich phase at high temperatures. A CALPHAD database built on an associate model is used to set up a ternary Cahn-Hilliard model, which can describe two-phase patterns in U-O-Zr. The interface structure and properties, which depend on the choice on the gradient energy coefficients in the free-energy functional, are studied in detail. It is found that interface adsorption is generally present due to the diffuse character of the interface, but that its magnitude is small, such that the model remains a robust and useful tool for future simulations of corium pool stratification dynamics.

Keywords: Cahn-Hilliard, CALPHAD, liquid phase segregation, multicomponent diffusion, U-O-Zr system, in-vessel corium

1. Introduction

During a severe accident in a light-water nuclear reactor, the meltdown of the reactor core can lead to the creation of *corium*, a mixture of the nuclear fuel, the cladding, and reactor components made of steel. Due to residual nuclear decays, the entire material produces heat, and can thus “melt its way” into the ground, where it can lead to major contamination of the environment. One way to avoid this is to retain the corium in the reactor vessel lower head by continuous cooling. For this so-called “In-Vessel Retention” strategy (IVR) [1], it is important to evaluate the heat flux that needs to be evacuated by the water circulating in the flooded reactor cavity.

The situation is complicated by the fact that corium exhibits two-phase coexistence between a metallic and an oxide phase, with very different heat conductivities, and densities that depend on the composition. The knowledge of the spatial distribution of these phases (the stratification of the corium pool) is important for a precise evaluation of the thermal transport. Various global scenarios for stratifications as well as hydrodynamic instabilities of the two-phase interfaces have been investigated by numerical models and model experiments. As discussed in [2] and further illustrated in [3] by code-to-code benchmarks, large uncertainties still exist in the quantitative assessment of such stratification transients and they have a strong impact on the overall evaluation of vessel wall melt-through under IVR conditions. In order to reduce this uncertainty, the few existing integral models [4, 5] that describe stratification transients in severe accident codes are in need for validation or parameter calibration. While small-scale experiments (using up to a few kilograms of prototypical materials e.g. depleted uranium) such as MASCA [6] and CORDEB [7] programs

*Corresponding author

Email address: mirantsoa-aime.rasolofomanana@cea.fr (M.A. Rasolofomanana)

20 are crucial to gain knowledge on the thermochemical effects at play for such systems, they cannot capture relevant hydrodynamic and thermal phenomena. In particular, considering stratification kinetics, only the medium-scale MASCA-RCW experiment [8] where 5 kg of molten steel were poured on top of about 45 kg of suboxidized corium has provided relevant information about the coupling between mass transfer and Rayleigh-Taylor instabilities at the interface between oxide and metal phases. Despite the possible new experiments [9] under study, it is important to note that experiments at nuclear reactor scale (tens of tons of materials, meter-scale length) cannot be conducted. Therefore, computational modelling is needed [10], and Computational Fluid Dynamics (CFD) simulations appear as an increasingly valuable tool in order to study pool thermal hydraulics [11, 12].

30 In this context, the long-term goal of our efforts is to formulate a model capable of simulating the dynamic evolution of the corium pool. Such a model needs to combine equations for heat and mass transfer (hydrodynamics) with a correct description of thermodynamic phases and interfaces. Diffuse-interface models are well suited for both purposes. They have become a standard method to simulate two-phase hydrodynamic flows [13], their advantage being to avoid the explicit tracking of the fluid-fluid interfaces. Furthermore, since such models are directly derived from out-of equilibrium thermodynamics, the correct two-phase equilibria are guaranteed. We have previously investigated the coupling with thermodynamic databases and two-phase hydrodynamics in simplified systems. A diffuse-interface model for the binary U-O system was developed in [14]. Phase separation was described by a Cahn-Hilliard equation for the concentration of U, coupled to a CALPHAD database. Furthermore, simulations of Rayleigh-Taylor instabilities were performed in a coupled Cahn-Hilliard/Navier-Stokes model, where the thermodynamics of corium was treated in a pseudobinary approximation [15], and it was shown that a such coupling can capture both the hydrodynamic phenomenon of a two-phase liquid pool and the thermochemical phenomenon (mass transfer).

40 The goal of the present work is the development and validation of a diffuse-interface model for the U-O-Zr system, which can be seen as a minimal model for corium, in the sense that it exhibits a liquid-liquid two-phase coexistence between a metal-rich and an oxide-rich phase. It is a further preliminary step towards the U-O-Zr-steel system that is representative for in-vessel corium. With respect to the simpler systems discussed above, the major new aspect is that there are now two independent concentration fields. This raises two new questions.

45 First, the thermodynamics of the U-O-Zr system is modeled in the CALPHAD approach by an associate model which involves the oxide species UO_2 and ZrO_2 in addition to the pure metals U and Zr, and we need to establish the link between this description and the diffuse-interface model that is formulated as two coupled Cahn-Hilliard equations for the concentrations of U and Zr. A new element here is that there is an internal degree of freedom, which simply reflects the fact that oxygen can associate with U or Zr, and that it can switch partners according to the thermodynamic conditions. This problem is solved by a dynamic local minimization procedure, that is, for each space point and at each time, the “inventory” of components is distributed between the different constituents such as to minimize the local free energy.

50 Second, the structure of the diffuse interfaces also needs to be investigated. Indeed, in a multi-component Cahn-Hilliard model, the interface profile is determined by the interplay of the composition-dependent bulk thermodynamic free energy and the so-called gradient energy coefficients, which penalize spatial variations of the composition. In an n -component system, there are $n(n - 1)/2$ such coefficients – three for the ternary case considered here. Physically, these coefficients are related to the interatomic interactions of the various species, but since no detailed information about the latter is available, there is no way to calculate the gradient energy coefficients *a priori*. Even if the interface free energy is known, this only yields one constraint, and the question then arises whether there exists an optimal choice for these coefficients.

55 This question is investigated in detail in the present paper. Progress can be made by taking into account the desirable properties of such a model. The model is intended to be used on the scale of two-phase patterns in corium, which are of the order of centimeters [8]. The thickness of the diffuse interfaces, which sets the mesh size for numerical discretization, has then to be chosen much larger than the physical interface thickness (typically nanometers). Therefore, complex interfacial profiles (such as non-monotonous concentration fields) should be avoided to prevent spurious couplings to the hydrodynamic flows. Furthermore, interfacial adsorption, that is, the accumulation of one or several components in the interface, can occur [16]. This natural physical effect can become a problem in numerical simulations, since it is also amplified by the

interface upscaling. Therefore, it should ideally be suppressed in the model. Finally, even though the lack of experimental data makes this difficult, a good agreement with interfacial energy data must be reached.

We investigate three different two-phase equilibria in the U-O-Zr system and systematically vary the gradient energy coefficients to study their influence on the interface structure and interface adsorption. We discuss various criteria for an optimal choice, but do not find a simple “recipe” that would ensure monotonous concentration profiles and the absence of interface adsorption. Since we thus have to accept “imperfect” interfaces, we evaluate numerically and analytically the consequences of interface upscaling, and find that the interface adsorption modifies the two-phase equilibria in systems of finite size. However, a scale separation between interface thickness and system size that is reasonable in terms of computational efficiency (one order of magnitude) yields shifts in equilibrium compositions of the order of only one percent. If such a precision is deemed sufficient, our model can then be used with any “reasonable” choice of the gradient energy coefficients.

The remainder of this paper is structured as follows. First, we define the diffuse-interface framework and detail the connection to the CALPHAD database. Then, we present numerical results for planar diffuse interfaces for several different two-phase equilibria, and discuss the influence of the gradient energy coefficients on the interface structure and interface adsorption. Finally, we study the influence of the finite interface thickness on two-phase equilibria in closed systems of finite size.

2. Ternary Cahn-Hilliard model

This section is devoted to the presentation of the diffuse-interface model proposed and studied in this work. In the following, isothermal conditions are considered and the dependency of all quantities on temperature T will be omitted for simplicity of notations.

2.1. Thermodynamic description of the U-O-Zr system

The phase diagram of the U-O-Zr system presents a liquid miscibility gap as shown on Figure 1. At thermodynamic equilibrium, an “oxidic” (L2) and a “metallic” liquid (L1) coexist.

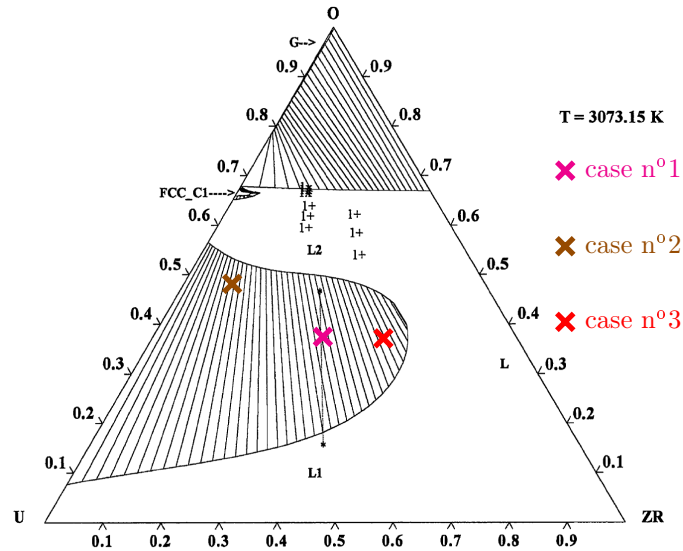


Figure 1: U-O-Zr phase diagram at temperature $T = 3073.15\text{K}$ and pressure of 1 bar (adapted from [17]) and locations associated with the system inventory for the different simulations of Section 3.

In the following, we will consider that the thermodynamic description of the U-O-Zr liquid phase is given by a Gibbs energy model through a CALPHAD database [18]. More precisely, for the sake of clarity of our

presentation, a non-ideal associate model will be considered where the associated variables are the molar fractions of the following five stoichiometric compounds: two oxide species (uranium dioxide UO_2 , zirconium dioxide ZrO_2), two metallic species (uranium U and zirconium Zr) and “free” oxygen O . Such a model is typically used in the NUCLEA database [19, 20] (from which our U-O-Zr thermodynamic representation has been extracted for numerical simulations) and is special case of the general Compound Energy Formalism (CEF) model where only one sublattice is considered and where, consequently, constituents and endmembers (in this case, the stoichiometric compounds) are one and the same. Note that the final form of the Cahn-Hilliard based model proposed in this paper is not limited to such an associate model.

In the following, we denote:

- $\{x_i\}_{i \in \mathcal{E}}$ the molar fraction of components and $\mathcal{E} = \{U, O, Zr\}$ the set of components;
- $\{y_i\}_{i \in \mathcal{S}}$ the molar fraction of constituents and $\mathcal{S} = \{\text{UO}_2, \text{ZrO}_2, U, Zr, O\}$ the set of constituents.

As a consequence, the CALPHAD thermodynamic representation of the liquid phase takes the form of a function representing the Gibbs energy per mole of species and denoted as:

$$G_M^{liq} : \{y_i\}_{i \in \mathcal{S}} \mapsto G \quad (1)$$

where G is in $\text{J} \cdot \text{mol}^{-1}$. From such a representation, another function representing the Gibbs energy per mole of components can be obtained:

$$G_m^{liq} : \{y_i\}_{i \in \mathcal{S}} \mapsto \frac{G_M^{liq}}{\mathcal{N}} (\{y_i\}_{i \in \mathcal{S}}) \quad (2)$$

where \mathcal{N} is the total amount of components per mole of constituents *i.e.* $\mathcal{N} = 3(y_{\text{UO}_2} + y_{\text{ZrO}_2}) + y_U + y_{Zr} + y_O$.

As the constituent molar fractions should obey $\sum_{i \in \mathcal{S}} y_i = 1$, a new function describing the same Gibbs energy per mole of components can be defined in terms of independent variables, eliminating for instance the UO_2 molar fraction and considering the associated restricted set of species $\tilde{\mathcal{S}} = \{\text{ZrO}_2, U, Zr, O\}$:

$$\tilde{G}_m^{liq} : \{y_i\}_{i \in \tilde{\mathcal{S}}} \mapsto G_m^{liq} \left(\{y_i\}_{i \in \tilde{\mathcal{S}}}, y_{\text{UO}_2} = 1 - \sum_{i \in \tilde{\mathcal{S}}} y_i \right) \quad (3)$$

When considering a severe accident in a light water reactor, the Zircaloy cladding are only partially oxidised during core degradation in such a way that the overall U-O-Zr corium composition is substoichiometric in oxygen *i.e.* $x_O \leq 2(x_U + x_{Zr})$. In this case, as illustrated in Table 1 through a particular equilibrium calculation performed with the OpenCalphad software [21], the two phases at thermochemical equilibrium in the liquid miscibility gap do not contain any “free” oxygen *i.e.* $y_O = 0$.

Table 1: Molar species fraction $y_i^{\alpha,eq}$ at thermodynamic equilibrium for $x_U = 0.35$, $x_{Zr} = 0.25$ and $T = 3000\text{K}$

Phase α	$y_{\text{UO}_2}^{\alpha,eq}$	$y_{\text{ZrO}_2}^{\alpha,eq}$	$y_U^{\alpha,eq}$	$y_{Zr}^{\alpha,eq}$	$y_O^{\alpha,eq}$
oxide	0.363	0.156	0.222	0.259	$< 5.0 \times 10^{-6}$
metal	0.046	0.066	0.463	0.425	$< 5.0 \times 10^{-7}$

Under such conditions, the thermodynamic state of the system is completely defined by the following three constituent molar fractions: y_U , y_{Zr} and y_{ZrO_2} . All these three variables are non-conserved during a stratification transient, but they can be used to express the conserved component molar fractions under the following form:

$$\begin{cases} x_U = \frac{1 - (y_{Zr} + y_{\text{ZrO}_2})}{1 - 2(y_U + y_{Zr})} \\ x_{Zr} = \frac{y_{Zr} + y_{\text{ZrO}_2}}{1 - 2(y_U + y_{Zr})} \end{cases} \quad (4)$$

As a consequence, in our diffuse interface model, we have retained x_U , x_{Zr} and y_{ZrO_2} as independent variables and considered that the thermodynamic state of the ternary system is described by the following function giving the Gibbs energy per mole of components:

$$\tilde{G}^{liq} : \{x_U, x_{Zr}, y_{ZrO_2}\} \mapsto \tilde{G}_m^{liq} \left(y_{ZrO_2}, y_U = \frac{3x_U + x_{Zr} - 1}{2(x_U + x_{Zr})} + y_{ZrO_2}, y_{Zr} = \frac{x_{Zr}}{x_U + x_{Zr}} - y_{ZrO_2}, y_O = 0 \right) \quad (5)$$

130 2.2. Additional hypothesis on the redox reactions kinetics

As x_U and x_{Zr} are conserved variables, a natural choice for describing their evolution as a function of time in the framework of a diffuse-interface description is to consider a Cahn-Hilliard model (as described in the next section). However, \tilde{G}^{liq} being also a function of the non-conserved variable y_{ZrO_2} , the formulation of a phase-field model for describing the phase segregation in such a system is not completely straightforward.

135 The extra degree of freedom associated with y_{ZrO_2} comes from the fact that component mass transfer between the two phases in the liquid miscibility gap of such a suboxidized system can induce modifications of the local equilibrium of the redox reaction $UO_2 + Zr \xrightleftharpoons[(2)]{(1)} ZrO_2 + U$. Therefore, the time evolution of this degree of freedom should follow a local reaction kinetics model. Formulating such a model for y_{ZrO_2} would require some quantitative knowledge about the reaction rate constant that is not available.

140 Fortunately, past experiments investigating the oxidation of corium by a gaseous atmosphere as reviewed in [22, 23] have shown that the overall oxidation kinetics is never limited by the oxidation reaction kinetics itself, but is controlled by the reactant transport to the reactive interface. As a consequence, we can make the approximation that local redox reaction equilibrium is maintained at all time. This is consistent with the fact that the associated local oxygen exchange mechanisms occur at the atomic scale.

145 Under this hypothesis of instantaneous local equilibrium of the redox processes, y_{ZrO_2} can be formally described by a function of x_U and x_{Zr} of the following form:

$$Y_{ZrO_2}^{eq} : \{x_U, x_{Zr}\} \mapsto y_{ZrO_2} \text{ s.t. } \frac{\partial \tilde{G}^{liq}}{\partial y_{ZrO_2}}(x_U, x_{Zr}, y_{ZrO_2}) = 0 \quad (6)$$

associated with the local minima of the molar Gibbs energy. Its numerical evaluation is depicted in Figure 2. Using this solution, the thermodynamic landscape is reduced to the following function:

$$\tilde{G}^{liq} : \{x_U, x_{Zr}\} \mapsto \tilde{G}^{liq}(Y_{ZrO_2}^{eq}(x_U, x_{Zr}), x_U, x_{Zr}) \quad (7)$$

that depends only on the two conserved variables x_U and x_{Zr} .

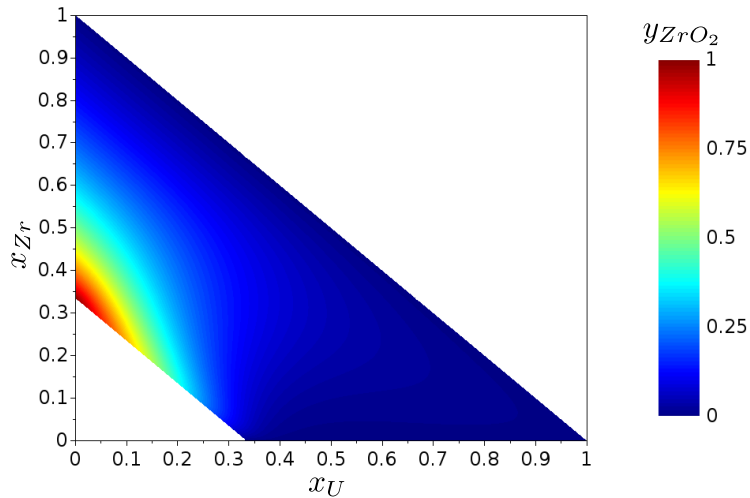


Figure 2: Illustration of $y_{ZrO_2} = Y_{ZrO_2}^{eq}(x_U, x_{Zr})$ associated with equilibrium of the redox reaction in the U-O-Zr system

150 Note that if this local redox equilibrium hypothesis was to be questioned in a later stage of this research work, the approach of [24] could be considered to extend the present model and properly define additional order parameters (obeying Allen-Cahn equations) to take into account the associated reaction kinetics. Some developments in this direction are further discussed in [25].

2.3. Governing equations

155 The evolution of x_U and x_{Zr} is described by two coupled Cahn-Hilliard equations under the classical hypothesis that the molar volume (denoted V_m) remains constant. More precisely, denoting Ω the spatial domain and $\partial\Omega$ its boundary, such equations for the order parameters x_U and x_{Zr} can be written as, $\forall i \in \{U, Zr\}$, $\forall \vec{r} \in \Omega$:

$$\frac{\partial x_i}{\partial t} = \nabla \cdot \left(\sum_{j \in \{U, Zr\}} \frac{\mathcal{M}_{i,j}}{a} \nabla \tilde{\mu}_j \right) \quad (8)$$

$$\tilde{\mu}_i = \frac{a}{V_m} \frac{\partial \bar{G}^{liq}}{\partial x_i} - \sum_{j \in \{U, Zr\}} \kappa_{i,j} \Delta x_j \quad (9)$$

160 supplemented by homogeneous Neumann conditions for x_i . For a closed system, the diffusion potentials $\tilde{\mu}_i$ are also subject to homogeneous Neumann conditions. The parameters associated with this model are:

- the symmetric kinetic coefficients $\{\mathcal{M}_{i,j}\}_{i,j \in \{U, Zr\}}$ to be related to component self-diffusion coefficients;
- a , an upscaling parameter which allows to treat a larger interface thickness than the characteristic length scale of the physical interface. As our model is intended for macroscopic simulations, we have considered large interface upscalings.
- 165 • $\bar{\kappa} = \{\kappa_{i,j}\}_{i,j \in \{U, Zr\}}$, the energy coefficients associated with the interfacial gradient terms $\nabla x_i \cdot \nabla x_j$ of the underlying free energy functional:

$$\mathcal{F} = \int_{\Omega} \left(\frac{1}{2} \sum_{i \in \{U, Zr\}} \sum_{j \in \{U, Zr\}} \kappa_{i,j} \nabla x_i \cdot \nabla x_j + \frac{a}{V_m} \bar{G}^{liq} \right) dV \quad (10)$$

They are discussed in details in the following sections. At this stage, one should note that a appears in the kinetic terms $\frac{\mathcal{M}_{i,j}}{a}$ of Eq. 8 in such a way that the macroscopic characteristic time τ obtained through non-dimensionalization of Eqs. 8 and 9 becomes independent of a *i.e.*

$$\tau = \frac{L_0^2 V_m}{\mathcal{M}_0 \bar{G}_0^{liq}} \quad (11)$$

170 considering characteristic length L_0 , mobility \mathcal{M}_0 and energy \bar{G}_0^{liq} . Indeed, in such a macroscopic model, the interface upscaling should not directly impact the transport of components in the bulk phases.

2.4. Kinetic parameters

175 In accordance with the general frame of linear phenomenological flux-force relationships [26], in the case of conservation equations expressed in terms of molar fractions and molar fluxes, the mobilities of Eq. 8 can be written as, $\forall i, j \in \{U, Zr\}$:

$$\mathcal{M}_{i,j} = \frac{V_m}{RT} \sum_{k \in \{U, Zr, O\}} (\delta_{j,k} - x_j)(\delta_{i,k} - x_i) x_k D_k \quad (12)$$

in terms of the component self-diffusion coefficients D_k and where δ is the Kronecker symbol. Following Onsager reciprocal relations, $\{\mathcal{M}_{i,j}\}_{i,j \in \{U,Zr\}}$ is symmetric. It means that

$$\mathcal{M}_{U,Zr} = \mathcal{M}_{Zr,U} = \frac{V_m}{RT} [-x_{Zr}(1-x_U)x_U D_U - x_U(1-x_{Zr})x_{Zr} D_{Zr} + x_U x_{Zr} x_O D_O] \quad (13)$$

In many Cahn-Hilliard based models, these so-called degenerate mobilities are replaced by average constant coefficients. In the present study, the explicit dependency on the order parameter values exhibited in Eq. 12 is kept in order to ensure that the local constituent molar fractions are kept in their associated physical range for all possible initial state of the system at all times. Such an approach is to be distinguished from Cahn-Hilliard models (typically for multiphase flows description e.g. [27]) where the thermodynamic landscape \bar{G}^{liq} and gradient energy coefficients $\kappa_{i,j}$ are constructed in order to ensure such constraints.

In particular, consistency of this ternary model with the underlying binary limiting cases is an important desired feature because of the component phase segregation in the initial state of the system (illustrated in Section 3). For instance, in the U-Zr case, the model should ensure that $\frac{\partial x_O}{\partial t} = 0$ in such a way that the two Cahn-Hilliard equations should give $\frac{\partial x_U}{\partial t} = -\frac{\partial x_{Zr}}{\partial t}$. Without further hypothesis on $\tilde{\mu}_i$, this is enforced if and only if $\mathcal{M}_{U,U} = -\mathcal{M}_{U,Zr} = -\mathcal{M}_{Zr,U} = \mathcal{M}_{Zr,Zr}$ in the ($x_O = 0$)-plane; one can easily verify that Eq. 12 satisfies this constraint.

Data on component self-diffusion coefficients D_k in molten corium mixtures are very scarce. In the following, for D_U and D_O , we have used the same data as in [14] (taken from molecular dynamics simulations of liquid UO_2 [28]) and taken D_{Zr} equal to D_U based on the fact that their atomic radii are close, $1.65 \pm 0.12\text{\AA}$ ($1.55 \pm 0.12\text{\AA}$) for U (resp. Zr). At $T = 3150\text{K}$, one obtains that $D_U = D_{Zr} = 1.9 \times 10^{-9}\text{m}^2\text{s}^{-1}$ and $D_O = 3.5 \times 10^{-9}\text{m}^2\text{s}^{-1}$.

2.5. Interface related parameters

As in our previous work on the binary U-O system [14], this model is intended for macroscopic scale simulations in such a way that it should be compatible with a large upscaling of the interface. In order to uncouple interface thickness and energy at steady state, the prefactor a is introduced in the thermodynamic landscape of Eq. 10 while, for the closure of the interface parameters $\bar{\kappa}$, the original intention is to use relevant information on the interfacial tension ¹. The associated issue of the data or models for evaluating interfacial energies in such complex systems was not addressed in this work and, accordingly, only constant gradient energy coefficients were considered.

Even under such an assumption the selection of $\bar{\kappa}$ is not straightforward. The surface energy can be calculated, but depends on the values of all the three independent gradient coefficients; thus, even if its value is known, two coefficients remain undetermined. However, thanks to the consistency with the limiting binary U-O case we want to enforce, the a and $\kappa_{U,U}$ coefficients can be unambiguously chosen. Indeed, in the U-O case, $\mathcal{M}_{U,Zr} = \mathcal{M}_{Zr,U} = \mathcal{M}_{Zr,Zr}$ are zero in such a way that x_{Zr} remains uniformly zero and Eqs. 8 and 9 for U are reduced to:

$$\frac{\partial x_U}{\partial t} = \nabla \cdot (\mathcal{M}_{U,U} \nabla \tilde{\mu}_U) \quad (14)$$

$$\tilde{\mu}_U = \frac{a}{V_m} \frac{\partial \bar{G}^{liq}}{\partial x_U} - \kappa_{U,U} \Delta x_U \quad (15)$$

In this specific case, considering a planar interface at steady state and assuming that far away from the interface, bulk molar fractions reach the thermodynamic equilibrium values, the same analytic expressions

¹This ‘‘top-down’’ approach for the model closure is to be distinguished from a ‘‘bottom-up’’ one where detailed microscopic information are used through a coarse graining procedure (see, for instance, [29]).

as in [14] are obtained for the interface thickness ε and interfacial tension σ_{UO} defined by:

$$\varepsilon = \frac{|x_U^{met,eq} - x_U^{ox,eq}|}{\max_{z \in \Omega} \left(\left| \frac{dx_U}{dz} \right| \right)} \quad (16)$$

$$\sigma_{UO} = \kappa_{U,U} \int_{\Omega} \left(\frac{dx_U}{dz} \right)^2 dz \quad (17)$$

i.e.

$$\varepsilon = \sqrt{\frac{\kappa_{U,U}}{2a}} A_{\varepsilon}^{eq} \quad (18)$$

$$\sigma_{UO} = \sqrt{2a\kappa_{U,U}} A_{\sigma}^{eq} \quad (19)$$

where A_{ε}^{eq} and A_{σ}^{eq} are constants that only depend on the thermodynamic equilibrium of the system in terms of the molar fractions $x_U^{\alpha,eq}$ and chemical potentials ($\mu_U^{\alpha,eq}, \mu_O^{eq}$) of the two coexisting phases $\alpha \in \{met, ox\}$. Such an equilibrium is completely defined by the temperature T and element inventory of the system in its initial state and can be evaluated through a Gibbs energy minimization procedure (as illustrated in Table 1). Accordingly, values for $\kappa_{U,U}$ and a can be explicitly evaluated as:

$$\kappa_{U,U} = \sigma_{UO} \varepsilon \frac{1}{A_{\varepsilon}^{eq} A_{\sigma}^{eq}} \quad (20)$$

$$a = \frac{\sigma_{UO}}{\varepsilon} \frac{A_{\varepsilon}^{eq}}{2A_{\sigma}^{eq}} \quad (21)$$

As in [14], σ_{UO} is crudely evaluated through the Girifalco model [30]:

$$\sigma_{UO} = \sigma_{UO_2/G} + \sigma_{U/G} - 2\sqrt{\sigma_{UO_2/G}\sigma_{U/G}} \quad (22)$$

under the constant molar volume hypothesis with liquid/gas surface tensions for pure liquid UO_2 ($\sigma_{UO_2/G}$) and U ($\sigma_{U/G}$) taken from [31]. At $T = 3200K$, it gives $\sigma_{UO} = 0.1N.m^{-1}$.

At this stage, the $\kappa_{Zr,Zr}$ and $\kappa_{U,Zr} = \kappa_{Zr,U}$ coefficients are left unspecified. While the overall idea would be to use them as additional degrees of freedom to be calibrated for prescribed configurations against interfacial energy data, as discussed in [25], such quantitative data for high-temperature corium systems are very scarce. Accordingly, in the following, the coefficients will be the subject of parametric studies.

3. Numerical results and discussion

In the following, we will study in detail the structure and properties of one-dimensional (1D) interfaces. After a discussion of the simulation setup in section 3.1, we will first look at interfaces in open systems, that is, with fixed chemical potentials and no constraints on the mass inventory. In this setting, the interfacial properties depend only on the free energy landscape and the gradient energy coefficients. We find it useful to start with a simple example in order to introduce the interface characteristics that are of interest. For this purpose, in section 3.2 we will consider the case $\bar{\kappa} = \kappa_{U,U}I$ (I being the 2×2 identity matrix) and discuss in details the interface profiles and the quantities of interest that can be used to describe interface properties. In section 3.3, we will then present a parametrization of $\bar{\kappa}$ and discuss its influence on the interface properties, with the goal to find an “optimal” set of gradient energy coefficients. Finally, closed systems of finite size will be investigated in section 3.4.

3.1. Simulation setup

The model has been implemented and tested for 1D slab geometries in a mock-up code. The spatial discretization is based on a simple staggered grid finite difference scheme that ensures stability while considering degenerate mobilities [32]. Time discretization is carried out by a fully implicit Euler scheme where

240 non-linearity is solved through Newton-Raphson iterations. Second-order derivatives of \bar{G}^{liq} involved in the system Jacobian are evaluated by finite difference formula based on the analytic evaluation of $\frac{\partial \bar{G}^{liq}}{\partial x_i}$.

Regarding these quantities, they have been obtained using the OpenCalphad code as interfaced (see [33]) in the PROCOR platform developed at CEA for corium propagation modelling [4]. Actually, two different approaches have been tested for this purpose. First, OpenCalphad was used to evaluate $\left\{ \frac{\partial \bar{G}^{liq}}{\partial y_j} \right\}_{j \in \mathcal{S}}$ and, 245 through the chain rule for derivatives, $\frac{\partial \bar{G}^{liq}}{\partial y_{ZrO_2}}$ in such a way that using the Brent's method, the root finding problem of Eq. 6 can be solved in order to construct $Y_{ZrO_2}^{eq}$ and, finally, evaluate $\left\{ \frac{\partial \bar{G}^{liq}}{\partial x_i} \right\}_{i \in \{U, Zr\}}$. Then, as a generalisation of the “local” equilibrium to any redox reactions, it was realised that such an hypothesis corresponds to Gibbs energy minimization for the liquid phase carried out discarding the possible phase separation associated with the miscibility gap. With OpenCalphad, such a calculation is made possible by 250 deactivating the so-called grid minimizer that is normally used to obtain an initial guess (in terms of phase compositions) for the iterative algorithm that searches for the global minimum; indeed, it is in this first step of a global equilibrium calculation that miscibility gaps are detected. As a consequence, for given x_U and x_{Zr} , such a local equilibrium calculation can be performed by OpenCalphad and associated component chemical potentials $\left\{ \mu_i^{loc. eq} \right\}$ can be directly retrieved in order to evaluate, $\forall i \in \{U, Zr\}$:

$$\frac{\partial \bar{G}^{liq}}{\partial x_i} = \left(\mu_i^{loc. eq} - \mu_O^{loc. eq} \right) \quad (23)$$

255 Note that the proposed model could be readily combined with surrogate models (e.g. neural networks as in [34]) of the thermodynamic landscape in order to avoid direct calls to a Gibbs energy minimizer and reduce the computational cost.

This model has been tested for different 1D configurations where two liquids are initially segregated in a system of size $L = h_{sup} + h_{inf}$ as depicted in Figure 3. Initial tests, not reported here for the sake of conciseness, were carried out in order to verify that the model behaves consistently when one of the 260 component is absent or when the overall inventory is such that the system is out of the miscibility gap; the reader is referred to [25] for more details. Then, different system compositions were chosen from the ternary phase diagram inside the miscibility gap (see Figure 1) in order to construct initial configurations presented in Table 2. Case n°1 is located in the central region of the miscibility gap while case n°2 (resp. case n°3) is in the U-rich (resp Zr-rich) region. In all cases, the temperature was set to $T = 3000K$ and the initial state corresponds to an oxide phase on top of a metallic phase. The interface was initialized with piecewise linear profiles of the molar fractions with at least six grid points in the interface.

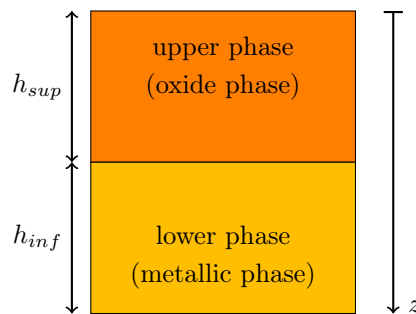


Figure 3: Schematics of the 1D simulation setup

Table 2: Parameters defining the initial system state for the different simulations

case	oxide phase		metallic phase	
	U molar fraction	Zr molar fraction	U molar fraction	Zr molar fraction
n°1	0.209	0.125	0.506	0.494
n°2	0.313	0.020	0.735	0.265
n°3	0.123	0.210	0.390	0.610

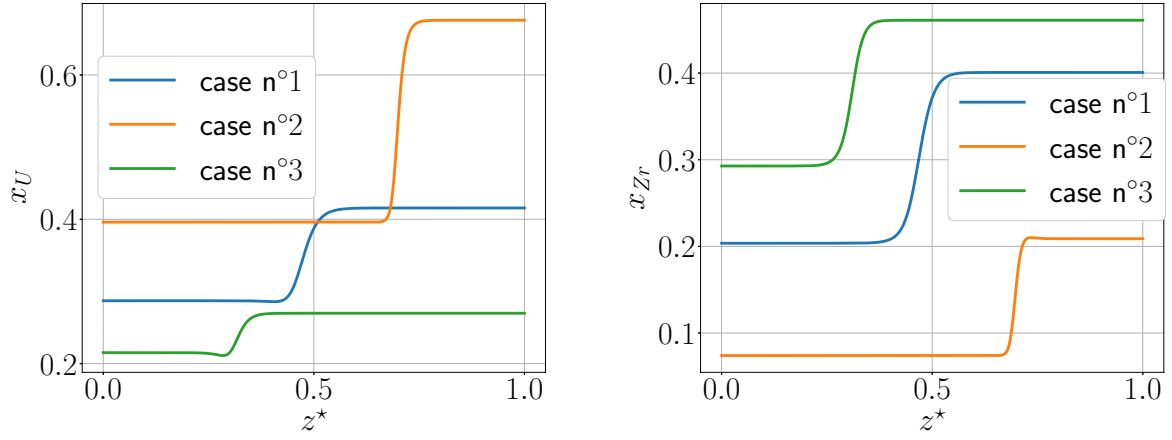
From Table 2, one can see that the metallic phase does not contain any oxygen (it contains only U and Zr). In all cases, σ_{UO} is kept equal to 0.1N.m^{-1} in such a way that the “free” model parameters are then ε , $\kappa_{Zr,Zr}$ and $\kappa_{U,Zr} = \kappa_{Zr,U}$. To keep the consistency with the binary system, a and $\kappa_{U,U}$ are obtained from Eqs. 20 and 21 based on σ_{UO} and ε .

In all the simulations, through sensitivities analyses, it was ensured that the numerical errors introduced by the time discretization along with the local minimization are at least one order of magnitude lower than the impact of these model parameters. The reader is referred to [25] for more details. The impact of the space discretization will be further discussed in Section 3.4.

3.2. Interface profiles and interface properties: an example case

While the interface solution in the case of binary systems is well known, the interfaces in ternary systems present some properties that are of importance and should therefore be discussed. In this section, after presenting interface profiles obtained using $\bar{\kappa} = \kappa_{U,U}I$, we discuss their properties, namely, their monotonicity and interface adsorption. In Figure 4 (a) and (b) the molar fractions of U and Zr are plotted as a function of z for the three different cases. First, since the interface is between an oxygen rich region to an oxygen poor region, both the molar fractions of U and Zr are increasing when going through the interface while the O molar fraction (not shown) is decreasing. As expected, one can also see that the magnitude of concentration changes depends on the position with respect to the miscibility gap while the interface thickness is similar in magnitude in the three cases. In addition, while in case 1 the concentration profiles are monotonous, one can see that in case 2 (resp. 3) the Zr (resp. U) profile is no longer monotonous and presents a clear maximum (resp. minimum) on the metallic (resp. oxide) side. This, in principle should not be an issue. However, this may lead to a non monotonous density profile when going through the interface and which may act as a source term for a Rayleigh-Taylor instability while bulk phases stratification is stable. Since we need to avoid such an unphysical behaviour, we need to prevent the formation of non monotonous profiles.

When considering in more details the interface structure, one can see that the apparent position of the interfaces for Zirconium and Uranium are not exactly the same and there is a small offset[16]. This is associated with interface adsorption as is explained in more details now.



(a) Uranium molar fraction profile

(b) Zirconium molar fraction profile

Figure 4: Steady-state molar fraction profiles for the three different cases of Table 2 with $\varepsilon = 4\text{mm}$ and $\bar{\kappa} = \kappa_{U,Zr}$.

In a diffuse interface approach, we can define \bar{x}_i as the average molar fraction of component i in the system by:

$$\bar{x}_i = \frac{1}{L} \int_0^L x_i dz \quad (24)$$

With an idealised zero-thickness interface, $\forall i \in \{U, Zr\}$, \bar{x}_i is a function of the position of this interface z_i^G that writes:

$$\bar{x}_i = \frac{z_i^G}{L} x_i^{ox} + \frac{L - z_i^G}{L} x_i^{met} \quad (25)$$

Eq. 25 for U and Zr components at equilibrium can be written as follow:

$$\begin{cases} \bar{x}_U = \frac{z_U^G}{L} x_U^{ox,eq} + \left(1 - \frac{z_U^G}{L}\right) x_U^{met,eq} \\ \bar{x}_{Zr} = \frac{z_{Zr}^G}{L} x_{Zr}^{ox,eq} + \left(1 - \frac{z_{Zr}^G}{L}\right) x_{Zr}^{met,eq} \end{cases} \quad (26)$$

Obviously, z_U^G and z_{Zr}^G are not necessarily equal. Therefore, we can define Δz^G as the distance between both interface positions:

$$\Delta z^G = z_U^G - z_{Zr}^G \quad (27)$$

The interface positions z_U^G , z_{Zr}^G , the distance Δz^G and the interface adsorption are illustrated qualitatively in Figure 5.

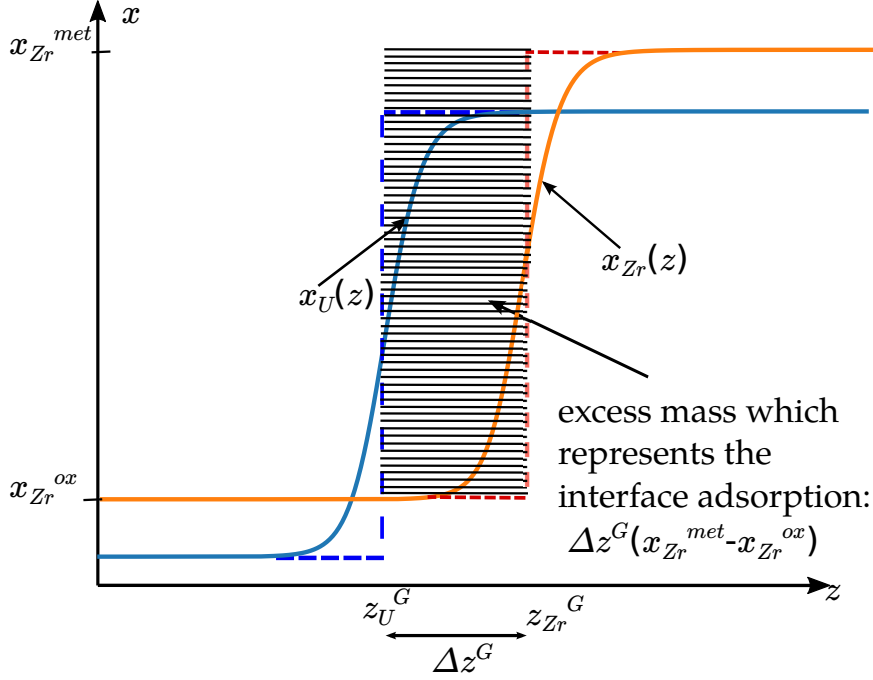


Figure 5: Illustration of the adsorption and the positions of the interface

It is important to note that, for our problem under imposed diffusion potentials $\tilde{\mu}_i$, the value of Δz^G depends on the interface thickness ϵ . To reduce this dependency, the following scaling $\tilde{z} = \frac{z}{\epsilon}$ can be introduced into the Cahn-Hilliard equation (Eq. 9) and leads to a system of equations for x_U and x_{Zr} that no longer directly depends on the interface thickness ϵ . Accordingly, the associated dimensionless quantity

$$\Delta \tilde{z}^G = \frac{\Delta z^G}{\epsilon} \quad (28)$$

only depends on $\bar{\kappa}$ and the thermodynamic landscape (through $\tilde{\mu}$) which implies that Δz^G is a linear function of ϵ as can be seen Figure 6. The expected linear trend is clearly shown with a slope that is directly $\Delta \tilde{z}^G$ and a convergence towards zero when $\epsilon = 0$ goes to zero.

From Eq. 26, by taking z_U^G as a reference for the interface position which is denoted z_{int} , \bar{x}_{Zr} can be written as a function of z_{int} and $\Delta \tilde{z}^G$:

$$\bar{x}_{Zr} = \left[\frac{z_{int}}{L} x_{Zr}^{ox,eq} + \left(1 - \frac{z_{int}}{L}\right) x_{Zr}^{met,eq} \right] + \frac{\epsilon}{L} \Delta \tilde{z}^G (x_{Zr}^{met,eq} - x_{Zr}^{ox,eq}) \quad (29)$$

In this expression, the second term of the r.h.s., $\frac{\epsilon}{L} \Delta \tilde{z}^G (x_{Zr}^{met,eq} - x_{Zr}^{ox,eq})$, corresponds to the contribution of the adsorption of Zr at the interface and varies linearly with $\frac{\epsilon}{L}$.

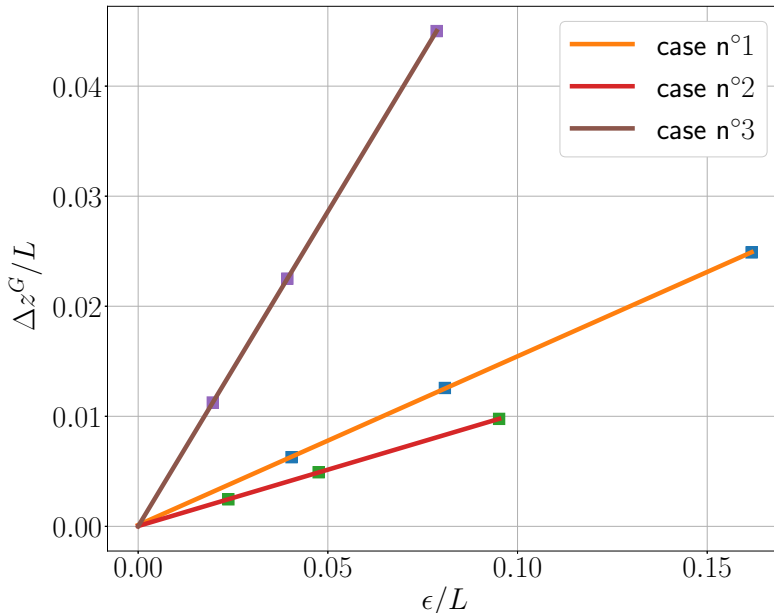


Figure 6: Interface position difference as a function of ϵ/L for different cases

Hence, for a non-zero interface thickness, surface adsorption is inevitable but can be minimized if $\Delta\tilde{z}^G$ is minimized. It should be noted that since the adsorption of the interface is proportional to $\Delta\tilde{z}^G$ between the positions of the interfaces for both components, the monotonicity of the interface profile is not directly linked to it. Accordingly, while a small value of $\Delta\tilde{z}^G$ is a desired model feature, it cannot be used as the only guideline for selecting the gradient coefficient parameters as it will not ensure monotonicity of the composition profiles.

All the discussion above has been focused on the convergence of the model and its applicability to large scale hydrodynamic simulations. However, an important feature of interfaces has not been discussed yet. Indeed we have not yet mentioned the surface tension or interface excess energy. This is an important property of the physical system since surface tension may (at least at small scales) have a significant impact on flow. However the lack of available data, makes it impossible to assess the quality of the model through comparison with model predictions. Nevertheless, it is an important aspect of the model and will be discussed in the following section. The interface energy was evaluated at equilibrium using the standard expression (see for instance [25]):

$$\sigma = \int_0^L \sum_{i \in \{U, Zr\}} \sum_{j \in \{U, Zr\}} \kappa_{i,j} \left(\frac{dx_i}{dz} \right) \left(\frac{dx_j}{dz} \right) dz \quad (30)$$

In the following section, we will examine how the changes in $\bar{\kappa}$ do affect the monotonicity, the interface adsorption and the surface tension. To this purpose, we use a simple parametrization of the $\bar{\kappa}$. Indeed, since $\bar{\kappa}$ is symmetric and positive, it can be decomposed as:

$$\bar{\kappa} = \alpha R D R^T \quad (31)$$

where R is a rotation matrix, R^T its transpose (and inverse), D a diagonal matrix and α is a prefactor chosen so that $\bar{\kappa}$ is consistent with the U-O binary system. In other words, $\kappa_{U,U}$ in ternary system should

be the same as $\kappa_{U,U}^{bin}$ calculated in the binary one. Accordingly, these quantities are defined by

$$R(\theta) = \begin{pmatrix} \cos \theta & -\sin \theta \\ \sin \theta & \cos \theta \end{pmatrix} \quad (32)$$

$$D(d) = \begin{pmatrix} 2 & 0 \\ 0 & d \end{pmatrix} \quad (33)$$

$$\alpha = \frac{\kappa_{U,U}^{bin}}{2 \cos^2 \theta + d \sin^2 \theta} \quad (34)$$

and this $\bar{\kappa}$ parameterization is fully defined by two coefficients: θ , the rotation angle and d , a diagonal coefficient that can be seen as a measure of anisotropy in the Gibbs triangle. From Eq. 31, it is clear that $\bar{\kappa}$ is a π -periodic function of θ and one can check that due to Eq. 34, $\bar{\kappa}(\theta + \pi, 4/d) = \bar{\kappa}(\theta, d)$. Therefore, the parametric study can be restricted to (d, θ) in the range $[0, 2] \times [0, \pi]$ without any loss of generality. One should also note that with $d = 0$, this decomposition is not valid when θ tends to $\frac{\pi}{2}$ since α diverges. We now describe the numerical results obtained. Since the monotonicity of the interface is a requirement, we will first discuss this point. Thereafter, we will discuss how the changes in d, θ affect the interface adsorption and the surface tension.

3.3. “Optimal” gradient energy coefficient matrix for a monotonous profile

The first criterion for choosing $\bar{\kappa}$ is the monotonicity of the composition profiles. From the various simulations performed, we have found that, at least in the situations studied here, increasing d , favoured the appearance of non monotonous profiles as can be seen in Figures 7 and 8 where, for a given value of $\theta = 45^\circ$, both uranium and zirconium molar fraction profiles are depicted when varying d in case n°2 and case n°3 respectively. In both cases, one can see that for higher values of d , there is an enrichment or depletion (non monotonicity of the molar fraction profile) in the minority phase. Zr-enrichment in the metallic phase for case n°2 and U-depletion in the oxide phase for case n°3 are increasing when d increases. This translates into the following properties:

- There exists a case dependent d -threshold value (denoted d_{lb}) above which there exists no θ value that can enforce monotonicity of the composition profiles. In case n°2 (resp. case n°3), d_{lb} is about 0.5 (resp. 0.2).
- For a given value of $d \leq d_{lb}$, there exists a θ -range in which monotonicity is ensured. This trend is illustrated in Figures 9 and 10 where the molar fraction profiles are depicted when varying $\theta \in [0, \pi[$ with $d = 0.5$ in case n°2 and $d = 0.2$ in case n°3 respectively. It can be observed that for $d = 0.5$ in case n°2, composition profiles of Zr are monotonous for $40^\circ \leq \theta \leq 70^\circ$ while in case n°3 for $d = 0.2$, composition profiles of U are monotonous for $0^\circ \leq \theta \leq 40^\circ$.

As a result, for each case there is a region of the *parameter range* for which the interface profile is monotonous. This range, at least here, corresponds to values of d below a threshold. In this domain, parameters should be chosen in order to both minimize interface adsorption that has adverse effects to convergence and to have a good approximation of surface tension. We first discuss the effect of the choice of $\bar{\kappa}$ on adsorption. Since, as following Eq. 28, the interface adsorption is linear with interface thickness, the quantity that must be minimized is the coefficient of proportionality, $\Delta \tilde{z}^G$. It has been evaluated in all calculations, regardless of the monotonicity of the profile, as illustrated in Figures 11a and 11b for both case n°2 and case n°3. For a given value of θ , in the range for which monotonicity is possible, it was found that $\Delta \tilde{z}^G$ decreases when d increases, which implies, that for a given value of θ , the best choice should be d_{lb} . When considering the variation of $\Delta \tilde{z}^G$ as a function of θ for a given value of d , one retrieves the expected π -periodic behaviour and one can see that the position of the extrema is case-dependent. However, it was found that in both cases, the position of the minimum was close to the monotonicity range. The examination of the amplitude of variation of $\Delta \tilde{z}^G$ is in our opinion of more interest. Indeed, in both cases, one can see that when varying d , its variations are rather small (about 10 to 20 %), when θ is varied, the changes can be much more significant

(from 50% to 8 fold). In addition, the changes are much stronger in case n°3 that corresponds to a situation closer to the *critical point*.

375 According to this analysis and the two associated criteria, the “optimal” choice of $\bar{\kappa}$ would then correspond to $d = 0.5$, $\theta = 70^\circ$ in case n°2 and $d = 0.2$, $\theta = 0^\circ$ in case n°3. As it could be anticipated, such an optimal choice is dependent on the tie-line under consideration. In addition, it must be noted that the discussion above has been focused on what we can call convergence aspects of the model and has not discussed the issue of the surface tension that is an important physical constant and can have dramatic effects such as Marangoni flows. This is mostly due to the lack of data on the surface tension. However, since the approach presented here is not limited to the context of corium, we find it necessary to discuss the effects of the choice of $\bar{\kappa}$ on the variation of surface tension.

380

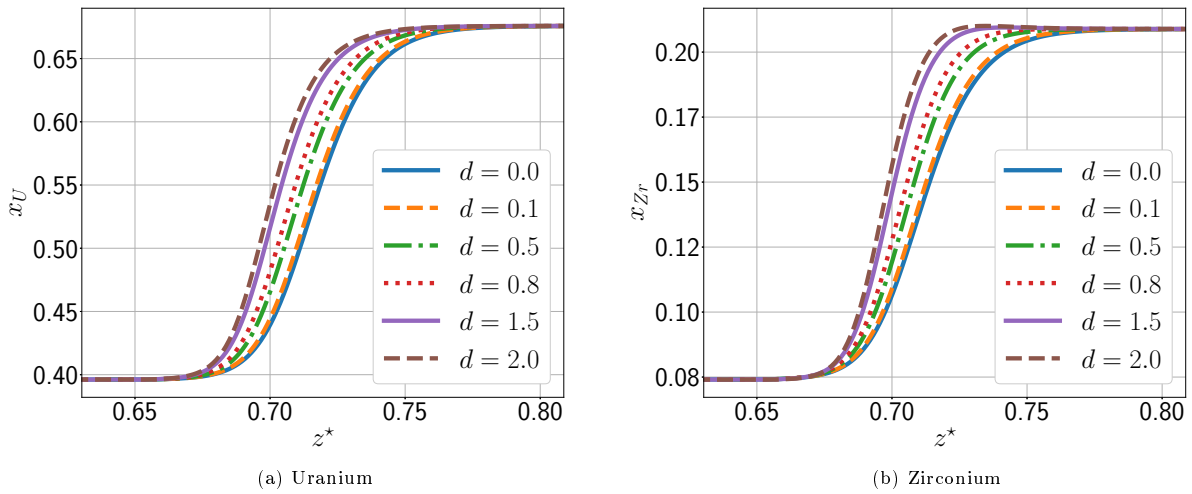


Figure 7: Steady-state molar fraction profiles for different values of d while keeping $\theta = 45^\circ$ in case n°2 of Table 2 with $\epsilon = 4\text{mm}$

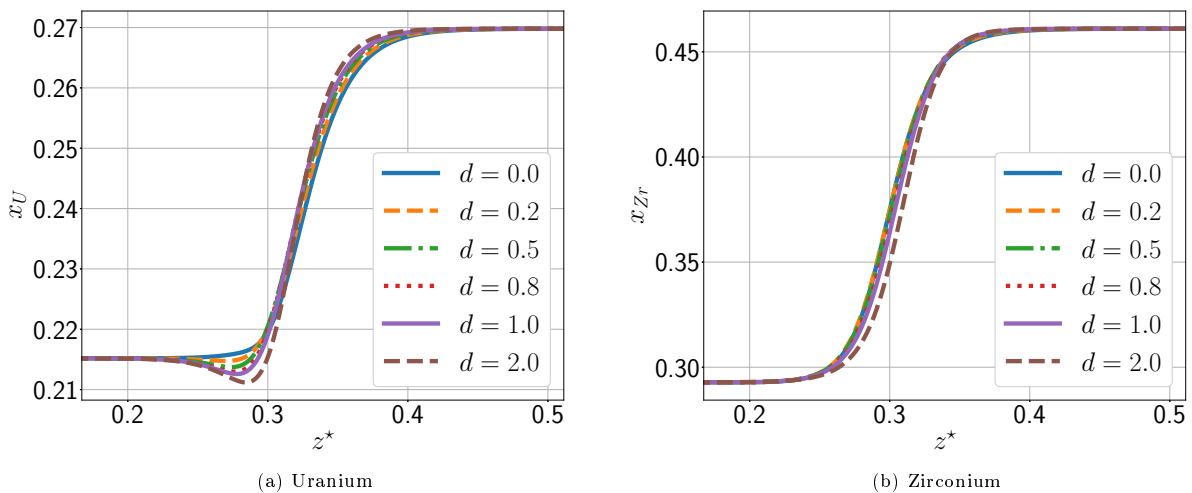


Figure 8: Steady-state molar fraction profiles for different values of d while keeping $\theta = 45^\circ$ in case n°3 of Table 2 with $\epsilon = 4\text{mm}$

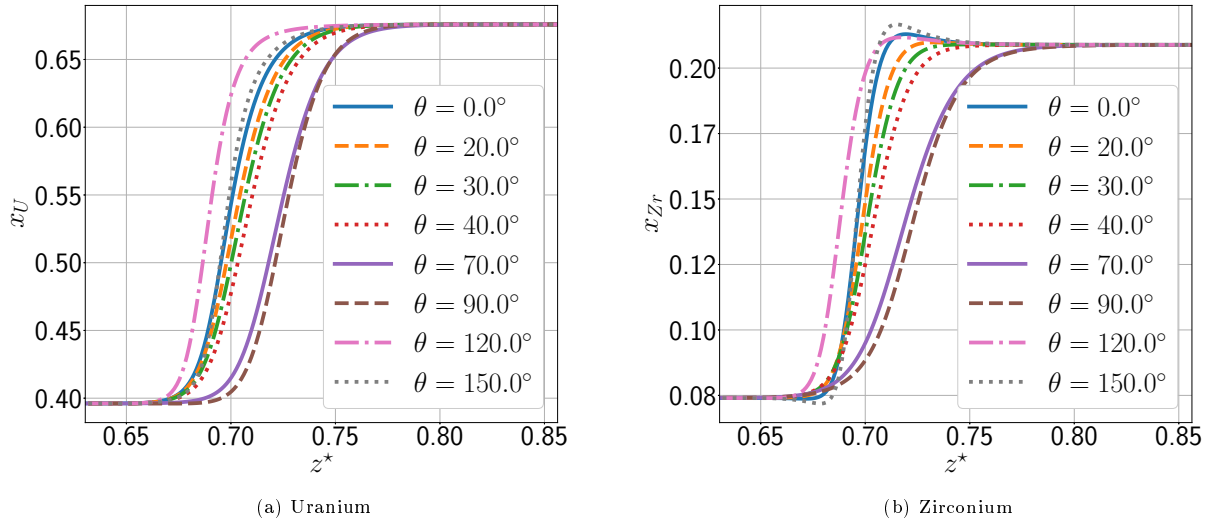


Figure 9: Steady-state molar fraction profiles for different values of θ while keeping $d = 0.5$ in case n² of Table 2 with $\epsilon = 4\text{mm}$

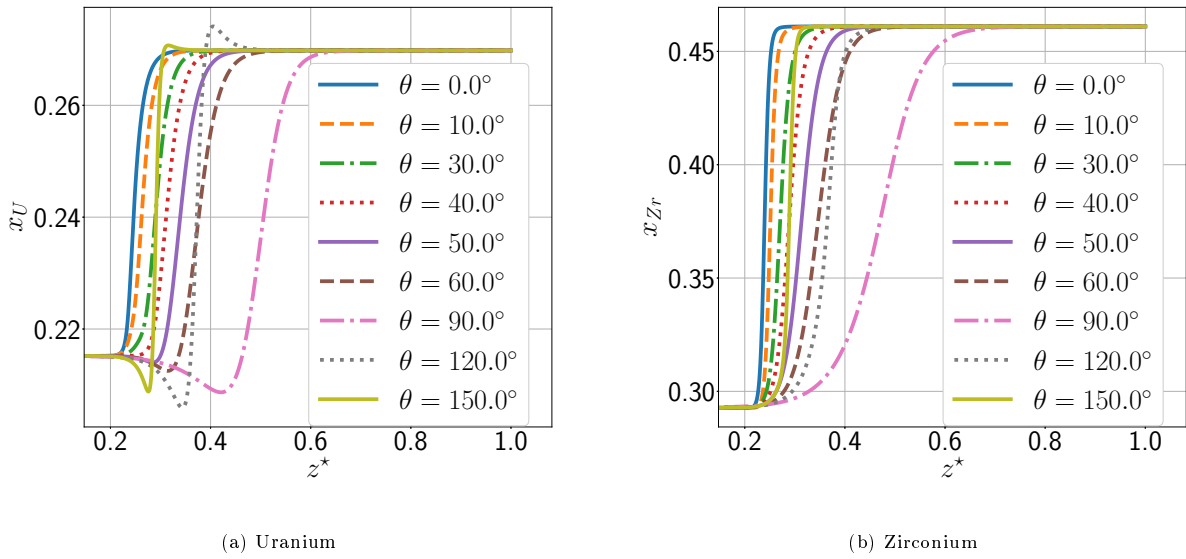


Figure 10: Steady-state molar fraction profiles for different values of θ while keeping $d = 0.2$ in case n³ of Table 2 with $\epsilon = 4\text{mm}$

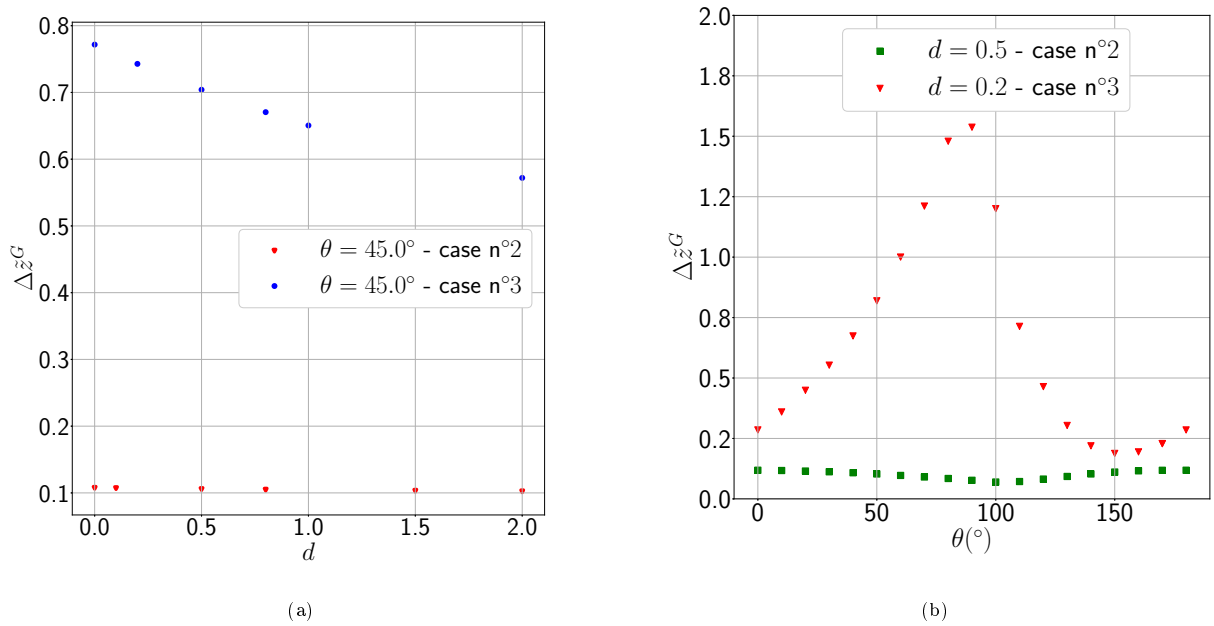


Figure 11: Scaled difference between interface positions of U and Zr as a function of d in (a) for the same value of $\theta = 45^\circ$ and cases 2 and 3. The same quantity is plotted in (b) as function of θ for $d = 0.5$ in case 2 and $d = 0.2$ in case 3

First, when considering a given θ angle, and varying d we find that σ is decreasing with d in both cases n°2 and n°3 in the range of θ for which monotonicity is possible. This behaviour is exemplified in Figure 12a where the surface tension is plotted as a function of d for $\theta = 45^\circ$. This may seem counterintuitive since increasing d is increasing the contribution of the squared gradient term to the surface energy. However, one should not forget that in order to keep consistency with the U-O case, the prefactor α is also varying when d is increasing. Therefore, it is not surprising that such dependency is observed. For a given value of d , the periodic behaviour of σ as a function of θ is also present. In both studied cases, $\sigma(\theta)$ presents a maximum close to $\theta = 75^\circ$. However, it is worth mentioning that while in both cases the magnitude of σ variations is similar (around $4 \cdot 10^{-2} \text{N.m}^{-1}$) the relative amplitude is much larger in the case n°3 which is closer to the critical point that is characterized by a zero surface tension. While with a knowledge of θ as a function of the tie line, such information would be crucial to choose the $\bar{\kappa}$, here it is of little help and cannot be further discussed. But this subject will have to be tackled in order to reach a quantitative description of flows since surface tension plays a significant role in multiphase hydrodynamics and in Rayleigh Taylor instabilities (see for instance [15]).

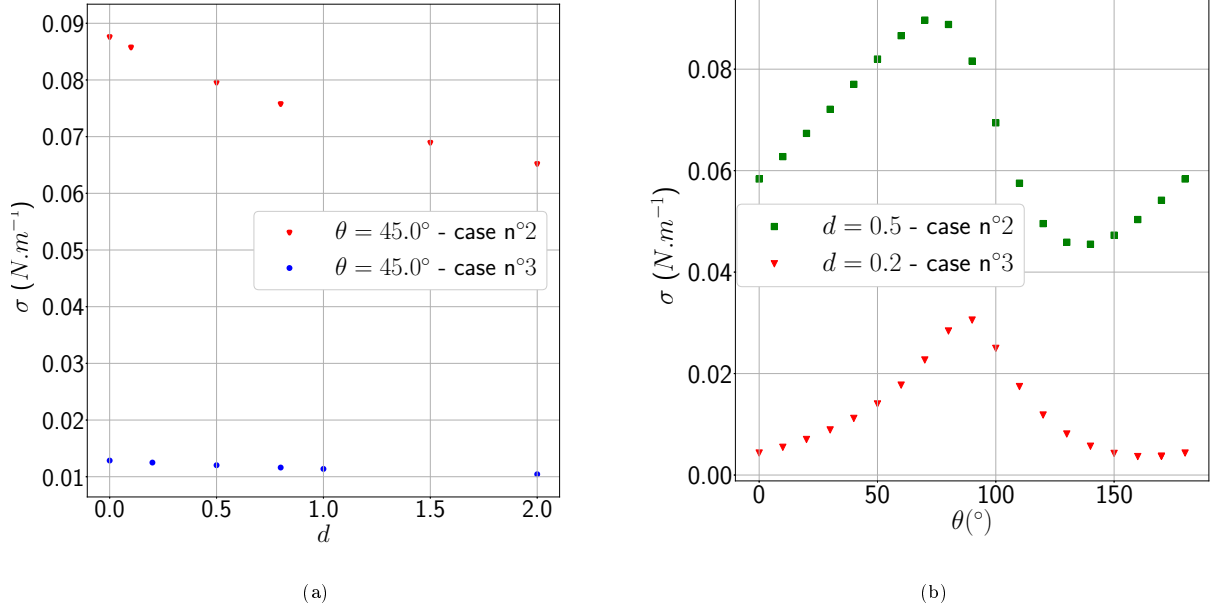


Figure 12: (a) Surface tension for different values of d with the same rotation angle $\theta = 45^\circ$ in cases 2 and 3. (b) Surface tension for different values of θ for given values of d in cases 2 and 3

Finally, as in [25], we depict the composition trajectory associated with the interfacial profiles in the thermodynamic landscape to highlight its impact. In Figure 13, for both cases n°2 and n°3 the energy density defined by

$$\frac{1}{V_m} \left(\bar{G}^{liq}(x_U, x_{Zr}) - \sum_{i \in \{U, Zr\}} (\mu_i^{eq} - \mu_O^{eq}) x_i \right) \quad (35)$$

is depicted with contour lines uniformly spaced every $6.0 \times 10^5 \text{ J} \cdot \text{m}^{-3}$. On this landscape, the trajectories corresponding to the interfacial profiles are plotted for different choices of $\bar{\kappa}$: a diagonal matrix with ($d = 2$ regardless of θ), a matrix where all the coefficients are equal ($d = 0, \theta = 45^\circ$) and the case-dependent “optimal” choice previously defined.

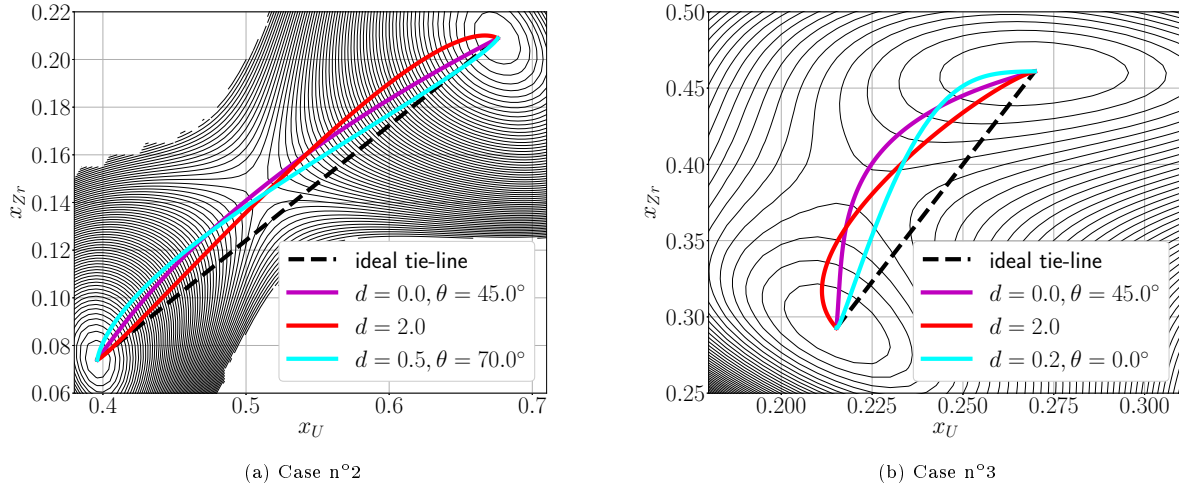


Figure 13: Steady-state interface profile x_{Zr} as a function of x_U superimposed over the thermodynamic landscape defined by Eq. 35 for different forms of $\bar{\kappa}$ at $\varepsilon = 4\text{mm}$ - contour lines associated with the energy density are uniformly spaced every $6.0 \times 10^5 \text{J}\cdot\text{m}^{-3}$

First, the lesser density of contour lines indicates that the thermodynamic landscape is more “flat” in case n°3 compared to case n°2: the minimum energy wells are less pronounced. In addition, the distance between bulk compositions is smaller. This is consistent with the fact the case n°3 is closer to the critical point than the case n°2 as can be seen in Figure 1. When considering interfaces paths, profiles present a deviation from the ideal tie line. This deviation presents two striking particularities. First, it is always passing in the vicinity of the saddle point of the energy landscape (the path) and the energy cost associated with any deviation from this path is apparently too costly. This entails that unless this path is close to the ideal tie line, the trajectory in the Gibbs triangle will not be close to the ideal tie line.

All previous calculations for discussing the choice of the gradient energy coefficients have been made considering Dirichlet boundary conditions for $\tilde{\mu}_i$, $\forall i \in \{U, Zr\}$, $\tilde{\mu}_i(0) = \tilde{\mu}_i(L) = \tilde{\mu}_i^{eq}$ in such a way that the problem to be numerically solved is simpler as it reduces Eq. 9 with $\tilde{\mu}_i = \tilde{\mu}_i^{eq}$. Indeed, such simulations pertaining to an open system are adequate to study the interface structure. However, when considering the simulation of a closed system, additional important bulk effects are to be taken into account. They will be discussed next.

3.4. Finite size problem

Unlike the imposed diffusion potential problem considered in the previous sections, the numerical solution of such a Cahn-Hilliard model for a closed system, as a reactor vessel, requires to impose no flux boundary conditions. In the case of the time-dependent Eqs. 8 and 9 this implies homogeneous Neumann boundary conditions for $\tilde{\mu}_i$. This system under mass conservation constraint is often referred to as *finite size* problem.

The same configurations as in Section 3.1 have been considered but only the results of case n°3 are reported because the non-monotonous effect was found the most severe in this case. As expected, the exact same behaviour as in Figure 4 is found for the composition profiles at steady state inside the interface zone for a given value of $\bar{\kappa}$. However the compositions far from the interface are not exactly the equilibrium ones and vary with the interface thickness. Figure 14 (resp. Figure 15) illustrates this by depicting the relative deviation Δx_U (resp. Δx_{Zr}) as a function of $\frac{\varepsilon}{L}$ for both the bulk oxide and metallic phases. This relative deviation is obtained by $\forall i \in \{U, Zr\}$ and $\forall k \in \{ox, met\}$,

$$\Delta x_i^k(\%) = 100 \times \frac{(x_i^{k,eq} - x_i^k)}{x_i^{k,eq}} \quad (36)$$

430 where $x_i^{k,eq}$ is the thermodynamic equilibrium value and x_i^k the actual computed value at steady-state.

435 These results are presented for different spatial meshes in order to check convergence with respect to discretization. When decreasing ε , the discrepancy w.r.t. thermodynamic equilibrium is reduced almost linearly and the asymptotic limit when $\frac{\varepsilon}{L} \rightarrow 0$ is found consistent with the overall equilibrium values providing that the spatial mesh is fine enough. The linear dependency in terms of $\frac{\varepsilon}{L}$ is observed for both U and Zr molar fractions. Uranium bulk composition is increasing with $\frac{\varepsilon}{L}$ while zirconium one is decreasing, which is consistent with the fact that Zirconium is adsorbed at the interface. The same variation (not shown here) is also noted for chemical potentials with respect to $\frac{\varepsilon}{L}$ since chemical potentials and compositions are linked by Eq. 9.

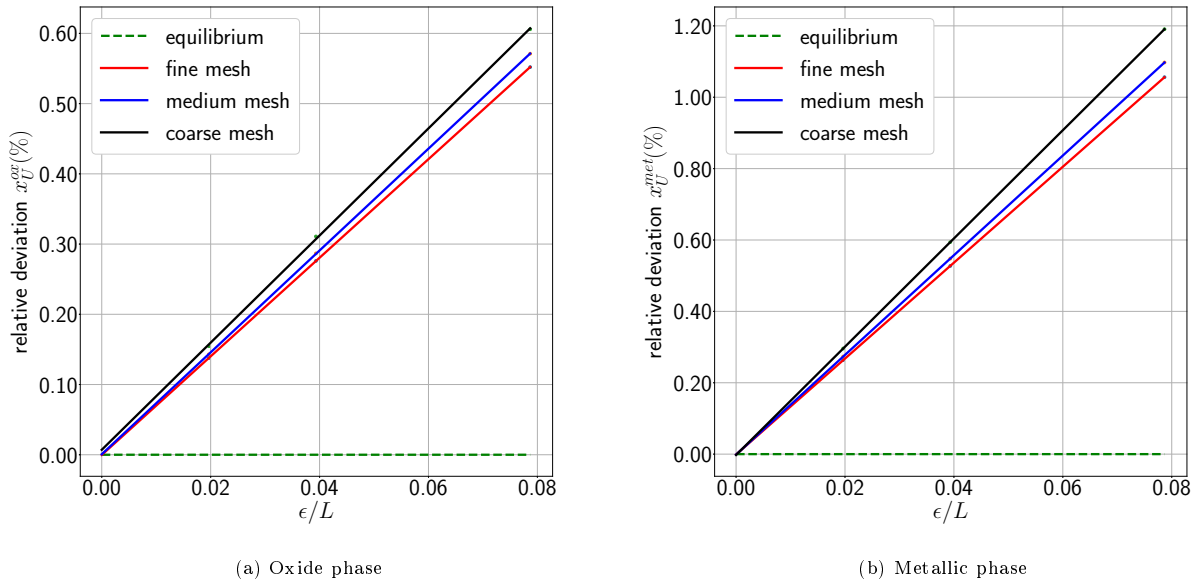


Figure 14: Relative deviation between equilibrium and Uranium composition from calculation at steady state as a function of ε/L for fine ($\Delta z = 10^{-4}$ m), medium ($\Delta z = 2 \times 10^{-4}$ m) and coarse mesh ($\Delta z = 4 \times 10^{-4}$ m) - case n°3

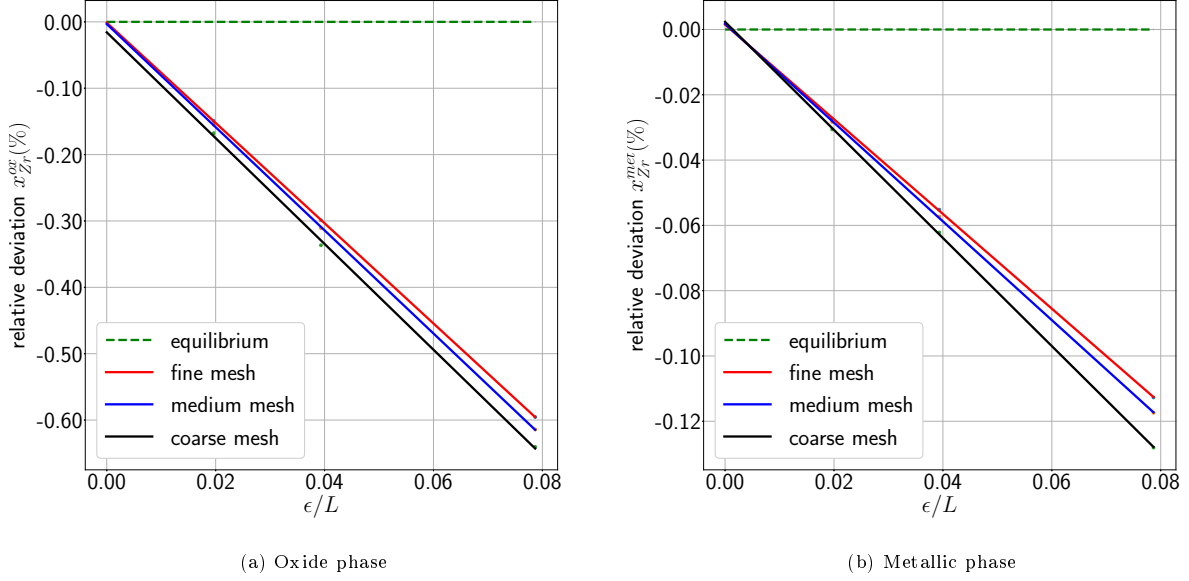


Figure 15: Relative deviation between equilibrium and Zirconium composition from calculation at steady state as a function of ϵ/L for fine ($\Delta z = 10^{-4}$ m), medium ($\Delta z = 2 \times 10^{-4}$ m) and coarse mesh ($\Delta z = 4 \times 10^{-4}$ m) - case n°3

In order to further discuss this asymptotic linear dependency, considering that the Gibbs energy is convex in the vicinity of the minimum energy wells, $\forall i \in \{U, Zr\}$ and $\forall k \in \{ox, met\}$, bulk compositions at steady state x_i^k are explicitly written as functions of the homogeneous diffusion potentials at steady state under the form $x_i^k = X_i^{k,eq}(\tilde{\mu}_U, \tilde{\mu}_{Zr})$ where $X_i^{k,eq}$ are thermodynamic functions that, for a given tie-line defined by $(\tilde{\mu}_U, \tilde{\mu}_{Zr})$, give the associated equilibrium compositions. Accordingly, for this finite size system, let us take the notation $\phi = \frac{z_U^G}{L}$, Eq. 29 becomes:

$$\begin{cases} \bar{x}_U = \phi X_U^{ox,eq}(\tilde{\mu}_U, \tilde{\mu}_{Zr}) + (1 - \phi) X_U^{met,eq}(\tilde{\mu}_U, \tilde{\mu}_{Zr}) \\ \bar{x}_{Zr} = \phi X_{Zr}^{ox,eq}(\tilde{\mu}_U, \tilde{\mu}_{Zr}) + (1 - \phi) X_{Zr}^{met,eq}(\tilde{\mu}_U, \tilde{\mu}_{Zr}) + \Delta z^G \frac{\epsilon}{L} [X_{Zr}^{met,eq}(\tilde{\mu}_U, \tilde{\mu}_{Zr}) - X_{Zr}^{ox,eq}(\tilde{\mu}_U, \tilde{\mu}_{Zr})] \end{cases} \quad (37)$$

Eq. 37 shows that the offset of Zr composition on the tie-line is conditioned by the interface thickness. In order to highlight this dependency of the bulk composition on the interface thickness ϵ , we can then proceed with a first-order asymptotic expansion in $\frac{\epsilon}{L}$ by considering

$$\begin{cases} \bar{x}_U = \bar{x}_U^0 + \frac{\epsilon}{L} \bar{x}_U^1 \\ \bar{x}_{Zr} = \bar{x}_{Zr}^0 + \frac{\epsilon}{L} \bar{x}_{Zr}^1 \\ \tilde{\mu}_U = \tilde{\mu}_U^{eq,0} + \frac{\epsilon}{L} \tilde{\mu}_U^{eq,1} \\ \tilde{\mu}_{Zr} = \tilde{\mu}_{Zr}^{eq,0} + \frac{\epsilon}{L} \tilde{\mu}_{Zr}^{eq,1} \\ \phi = \phi^0 + \frac{\epsilon}{L} \phi^1 \end{cases} \quad (38)$$

where the exponent “0” is used to denote the asymptotic limit of the different quantities when $\frac{\epsilon}{L} = 0$ *i.e.* the thermodynamic equilibrium values². Accordingly, $\forall i \in \{U, Zr\}$ and $\forall k \in \{ox, met\}$, the first-order expansion of $X_i^{k,eq}$ is then given by

$$X_i^{k,eq}(\tilde{\mu}_U, \tilde{\mu}_{Zr}) = x_i^{k,eq,0} + \frac{\epsilon}{L} \left(\left. \frac{\partial X_i^{k,eq}}{\partial \tilde{\mu}_U} \right|_0 \tilde{\mu}_U^{eq,1} + \left. \frac{\partial X_i^{k,eq}}{\partial \tilde{\mu}_{Zr}} \right|_0 \tilde{\mu}_{Zr}^{eq,1} \right) \quad (39)$$

²Note that, in Section 3.2, such an exponent “0” was not used as it would have been redundant with the “eq” exponent; the reader should keep in mind this difference in the notations between these two sections.

In the first-order expansion of Eq. 39, one can see that the convergence w.r.t. $\frac{\epsilon}{L}$ directly depends on the inverse of the Hessian matrix of the Gibbs energy function so that the convergence rate directly depends on the curvature of thermodynamic landscape in the vicinity of the minimum energy wells. Consistently with the discussion of Figure 13, it was observed that it is in case n°3 where the landscape is more flat that the effect of a non zero interface thickness of the bulk composition is more pronounced.

Then, to complete this asymptotic expansion, Eqs. 38 and 39 are injected in Eq. 37 and we obtain:

$$\begin{cases} \bar{x}_U^0 &= \phi^0 x_U^{ox,eq,0} + (1 - \phi^0) x_U^{met,eq,0} \\ \bar{x}_{Zr}^0 &= \phi^0 x_{Zr}^{ox,eq,0} + (1 - \phi^0) x_{Zr}^{met,eq,0} \end{cases} \quad (40)$$

and

$$\begin{cases} \bar{x}_U^1 &= \phi^0 \left(\frac{\partial X_U^{ox,eq}}{\partial \bar{\mu}_U} \Big|_0 \tilde{\mu}_U^{eq,1} + \frac{\partial X_U^{ox,eq}}{\partial \bar{\mu}_{Zr}} \Big|_0 \tilde{\mu}_{Zr}^{eq,1} \right) + (1 - \phi^0) \left(\frac{\partial X_U^{met,eq}}{\partial \bar{\mu}_U} \Big|_0 \tilde{\mu}_U^{eq,1} + \frac{\partial X_U^{met,eq}}{\partial \bar{\mu}_{Zr}} \Big|_0 \tilde{\mu}_{Zr}^{eq,1} \right) \\ &+ \phi^1 (x_U^{ox,eq,0} - x_U^{met,eq,0}) \\ \bar{x}_{Zr}^1 &= \phi^0 \left(\frac{\partial X_{Zr}^{ox,eq}}{\partial \bar{\mu}_U} \Big|_0 \tilde{\mu}_U^{eq,1} + \frac{\partial X_{Zr}^{ox,eq}}{\partial \bar{\mu}_{Zr}} \Big|_0 \tilde{\mu}_{Zr}^{eq,1} \right) + (1 - \phi^0) \left(\frac{\partial X_{Zr}^{met,eq}}{\partial \bar{\mu}_U} \Big|_0 \tilde{\mu}_U^{eq,1} + \frac{\partial X_{Zr}^{met,eq}}{\partial \bar{\mu}_{Zr}} \Big|_0 \tilde{\mu}_{Zr}^{eq,1} \right) \\ &+ \phi^1 (x_{Zr}^{ox,eq,0} - x_{Zr}^{met,eq,0}) + \Delta \tilde{z}^G (x_{Zr}^{met,eq,0} - x_{Zr}^{ox,eq,0}) \end{cases} \quad (41)$$

For a closed system, \bar{x}_U and \bar{x}_{Zr} are imposed so that \bar{x}_U^1 and \bar{x}_{Zr}^1 are 0. Then, to obtain a closed linear system of equations for $\{\tilde{\mu}_U^{eq,1}, \tilde{\mu}_{Zr}^{eq,1}, \phi^1\}$, the two equations 41 should to be supplemented by the following Clausius-Clapeyron relation

$$\frac{\tilde{\mu}_U^{eq,1}}{\tilde{\mu}_{Zr}^{eq,1}} = \frac{x_{Zr}^{met,eq,0} - x_{Zr}^{ox,eq,0}}{x_U^{ox,eq,0} - x_U^{met,eq,0}} \quad (42)$$

that directly comes from the fact that the grand potential is uniform at equilibrium. The numerical solution of this system was not evaluated in the present study but it is sufficient to note that the solution $\{\tilde{\mu}_U^{eq,1}, \tilde{\mu}_{Zr}^{eq,1}, \phi^1\}$ of this system is directly proportional to $\Delta \tilde{z}^G$ and, accordingly, becomes $\{0, 0, 0\}$ if $\Delta \tilde{z}^G$ is 0. In other words, the rate of convergence w.r.t. $\frac{\epsilon}{L}$ of all quantities of interest (chemical potentials, bulk compositions) is proportional to the adsorption-related term $\Delta \tilde{z}^G$ that solely depends on the thermodynamic landscape and the $\bar{\kappa}$ matrix. As such, it reinforces the interest of considering the minimization of $\Delta \tilde{z}^G$ as a criterion in the choice of $\bar{\kappa}$ as discussed in Section 3.3.

With that said, it should be noted that the discrepancy that is observed in Figures 14 and 15 remains limited (at the most of the order of 1% for a scale separation of about 0.08) and, from this point of view, the model appears as very robust when considering very large interface upscaling. This is a very important feature when considering the anticipated application of such model for corium stratification simulation. For instance, in the simulations reported in [15], qualitatively representative of the MASCA-RCW stratification transient, a scale separation of about 0.05 was used.

4. Conclusions and perspectives

In this paper, a model of the isothermal multicomponent mass transfer in a 1D configuration composed of two immiscible segregated phases has been proposed considering the liquid miscibility gap of the U-O-Zr ternary system of interest in the frame of in-vessel corium pool stratification analysis. A diffuse interface model has been proposed where Cahn-Hilliard equations describing the U and Zr molar fractions evolution are supplemented by a local equilibrium hypothesis regarding the redox reaction $UO_2 + Zr \xrightleftharpoons[(2)]{(1)} ZrO_2 + U$ in such a way that the thermodynamic landscape can be directly related to the Gibbs energy model of the liquid phase given by a CALPHAD database. As this model is intended to be used at a macroscopic level, an interface upscaling procedure, as previously introduced in our work on the U-O system, was considered. Enforcing consistency with the limiting binary U-O case, one out the three gradient energy coefficients associated with the model parameterization was obtained analytically along with the upscaling parameter as a function of the interface thickness and energy in this binary limiting case. Then, numerical

results have been presented focusing first on the impact that the other gradient energy coefficients have on the composition profiles at steady-state. The analysis was performed in terms of the monotonicity of the upscaled composition profiles and the interface adsorption (as characterized by the Gibbs construction) in such a way that case-dependent “optimal” parameters were defined. Additional numerical results were also reported illustrating the so-called “finite size” effect when bulk compositions at steady-state are compared with the thermodynamic equilibrium values as a function of the interface thickness. It was shown that our model is asymptotically consistent and that even when rather low scale separation are considered, the discrepancy w.r.t the thermodynamic limit remains limited (of the order of 1%). Accordingly, even if the model parameterization is not straightforward, it is a very good candidate for coupling with hydrodynamics in order to simulate multiphase corium stratification. Regarding this long-term research avenue, it is interesting to note that under the hypothesis of local redox reaction instantaneous equilibrium, the generalisation of this ternary model to any n -ary system composed of $n - 1$ metallic components and oxygen is straightforward in such a way that it can be applied to the U-O-Zr-steel system [25]. In this context, to follow-up on [15], the next step will be to introduce such a model in a “Computational Fluid Dynamics” code to further assess its ability to quantitatively describe the coupling between hydrodynamics and mass transfer in the peculiar corium pool system.

5. Data availability

Data presented in this manuscript will be made available upon request to the corresponding author.

Acknowledgements

This work has been carried out within the framework of the PROCOR platform development funded by CEA, EDF and Framatome. The authors would like to acknowledge B. Sundman for his help regarding the OpenCalphad software in the earliest stage of this project.

References

- [1] H. Tuomisto, T. G. Theofanous, A consistent approach to severe accident management, *Nuclear Engineering and Design* 148 (2) (1994) 171 – 183 (1994).
- [2] F. Fichot, L. Carénini, R. L. Tellier, L. Viot, N. Bakouta, A. Filippov, Identification and evaluation of the remaining uncertainties for transient situations (2020) 7 (2020).
- [3] L. Carénini, F. Fichot, N. Bakouta, A. Filippov, R. Le Tellier, L. Viot, I. Melnikov, P. Pandazis, Main outcomes from the IVR code benchmark performed in the European IVMR project, *Annals of Nuclear Energy* 146 (2020) 107612 (Oct. 2020). doi:10.1016/j.anucene.2020.107612.
URL <https://linkinghub.elsevier.com/retrieve/pii/S0306454920303108>
- [4] R. Le Tellier, L. Saas, F. Payot, Phenomenological analyses of corium propagation in LWRs: the PROCOR software platform, in: Proc. of the 7th European Review Meeting on Severe Accident Research ERMSAR-2015, Marseille, France, 2015 (2015).
- [5] L. Carénini, F. Fichot, Evaluation of the kinetics of molten pool stratification in case of In-Vessel Melt Retention Strategy, in: Proc. of 26th International Conference on Nuclear Engineering ICONE 26, London, England, 2018 (2018).
- [6] D. F. Tsurikov, V. F. Strizhov, S. V. Bechta, V. N. Zagriazkin, N. P. Kiselev, Main Results of MASCA1 and 2 Projects, Tech. rep., RRC Kurchatov Institute (2007).
- [7] V. I. Almajashev, V. S. Granovsky, V. B. Khabensky, S. Y. Kotova, E. V. Krushinov, A. A. Sulatsky, S. A. Vitol, V. V. Gusarov, F. Fichot, B. Michel, P. Piluso, R. Le Tellier, M. Fischer, C. Le Guennic, N. Bakouta, Experimental study of transient phenomena in the three-liquid oxidic-metallic corium pool, *Nuclear Engineering and Design* 332 (2018) 31 – 37 (2018).
- [8] V. G. Asmolov, S. S. Abalin, Y. A. Veselkin, V. Y. Vishnevsky, V. V. Vlasov, B. L. Gershman, Y. G. Degaltsev, Y. K. Dyakov, J. F. Isaev, A. N. Kiselev, N. P. Kiselev, A. M. Kovalev, A. G. Ol'khovskiy, K. V. Pechalin, L. M. Semenov, V. F. Strizhov, T. V. Trushkina, V. S. Uglov, Y. M. Utkin, V. V. Chudanov, A. E. Aksenova, V. A. Pervichko, L. M. Khazanivich, RCW Post-Test Analysis Results, Technical Report MP-TR-11, Russian Research Centre Kurchatov Institute (2003).
- [9] D. Tisseur, M. Cavaro, F. Rey, K. Paumel, N. Chikhi, J. Delacroix, P. Fouquart, R. Le Tellier, V. Bouyer, Study of online measurements techniques of metallic phases spatial distribution into a corium pool, in: Proc. of Int. Conf. on Advancements in Nuclear Instrumentation Measurement Methods and their Applications. ANIMMA 2019, Portoröz, Slovenia, 2019 (2019).

- [10] S. Nandan, Modélisation de la Dissolution d'une Phase Solide (UO₂ - ZrO₂ - Zr) par une Phase Liquide (Fe) par une Approche Macroscopique Diphasique, Ph.D. thesis, Université d'Aix-Marseille, LEPC - IRSN (2019).
- [11] A. Shams, D. Dovizio, K. Zwijssen, C. L. Guennic, L. Saas, R. Le Tellier, M. Peybernes, B. Bigot, E. Skrzypek, M. Skrzypek, L. Vyskocil, L. Carenini, F. Fichot, Status of computational fluid dynamics for in-vessel retention: Challenges and achievements, *Annals of Nuclear Energy* 135 (2020) 107004 (2020).
- [12] L. Zhang, Y. Zhou, S. Luo, Y. Zhang, G. H. Su, Z. Ma, L. Pan, Large eddy simulation for the thermal behavior of one-layer and two-layer corium pool configurations in HPR1000 reactor, *Applied Thermal Engineering* 145 (2018) 38 – 47 (2018).
- [13] D. M. Anderson, G. B. McFadden, A. A. Wheeler, Diffuse-interface methods in fluid mechanics, *Annual Review of Fluid Mechanics* 30 (1) (1998) 139–165 (1998). [arXiv:https://doi.org/10.1146/annurev.fluid.30.1.139](https://doi.org/10.1146/annurev.fluid.30.1.139), doi:10.1146/annurev.fluid.30.1.139.
URL <https://doi.org/10.1146/annurev.fluid.30.1.139>
- [14] C. Cardon, R. Le Tellier, M. Plapp, Modelling of Liquid Phase Segregation in the Uranium-Oxygen Binary System, *CALPHAD: Computer Coupling of Phase Diagrams and Thermochemistry* 52 (2016) 47–56 (2016).
- [15] R. Zanella, G. Tegze, R. Le Tellier, H. Henry, Two- and three-dimensional simulations of Rayleigh–Taylor instabilities using a coupled Cahn–Hilliard/Navier–Stokes model, *Physics of Fluids* 32 (124115) (2020). doi:10.1063/5.0031179.
URL <http://aip.scitation.org/doi/10.1063/5.0031179>
- [16] C. Huang, M. Olvera De La Cruz, P. W. Voorhees, Interfacial adsorption in ternary alloys, *Acta Materialia* 47 (17) (1999) 4449–4459 (1999). doi:10.1016/S1359-6454(99)00229-3.
- [17] P.-Y. Chevalier, E. Fischer, B. Cheynet, Progress in the thermodynamic modelling of the O-U-Zr ternary system, *Calphad* 28 (1) (2004) 15–40 (2004).
- [18] H. Lukas, S. G. Fries, B. Sundman, *Computational Thermodynamics: The Calphad Method*, Cambridge University Press, 2007 (2007).
- [19] B. Cheynet, P. Chevalier, E. Fischer, *Thermosuite*, *Calphad* 26 (2) (2002) 167–174 (2002).
- [20] S. Bakardjjeva, M. Barrachin, S. Bechta, D. Bottomley, L. Brissonneau, B. Cheynet, E. Fischer, C. Journeau, M. Kiselova, L. Mezentseva, P. Piluso, T. Wiss, Improvement of the European thermodynamic database NUCLEA, *Progress in Nuclear Energy* 52 (1) (2010) 84–96 (2010).
- [21] B. Sundman, U. R. Kattner, M. Palumbo, S. G. Fries, *OpenCalphad - a free thermodynamic software*, *Integrating Materials and Manufacturing Innovation* 4 (1) (2015).
- [22] A. A. Sulatsky, S. A. Smirnov, V. S. Granovsky, V. B. Khabensky, E. V. Krushinov, S. A. Vitol, S. Y. Kotova, M. Fischer, S. Hellmann, W. Tromm, A. Miassoedov, D. Bottomley, P. Piluso, M. Barrachin, Oxidation kinetics of corium pool, *Nuclear Engineering and Design* 262 (2013) 168 – 179 (2013).
- [23] V. I. Almyashev, V. S. Granovsky, V. B. Khabensky, E. V. Krushinov, A. A. Sulatsky, S. A. Vitol, V. V. Gusarov, S. Bechta, M. Barrachin, F. Fichot, P. D. Bottomley, M. Fischer, P. Piluso, Oxidation effects during corium melt in-vessel retention, *Nuclear Engineering and Design* 305 (2016) 389 – 399 (2016).
- [24] Y. Ji, H. W. Abernathy, L.-Q. Chen, Thermodynamic models of multicomponent nonstoichiometric solution phases using internal process order parameters, *Acta Materialia* 223 (2022) 117462 (Jan. 2022). doi:10.1016/j.actamat.2021.117462.
URL <https://www.sciencedirect.com/science/article/pii/S1359645421008417>
- [25] C. Cardon, Modélisation de la diffusion multi-composants dans un bain de corium diphasique oxyde-métal par une méthode d'interface diffuse, Ph.D. thesis, Université Paris-Saclay (2016).
- [26] J.-O. Andersson, J. Ågren, Models for numerical treatment of multicomponent diffusion in simple phases, *Journal of Applied Physics* 72 (4) (1992) 1350–1355 (Aug. 1992). doi:10.1063/1.351745.
URL <http://aip.scitation.org/doi/10.1063/1.351745>
- [27] C. Lapuerta, Echanges de masse et de chaleur entre les deux phases liquides stratifiées dans un écoulement à bulles, PhD Thesis, Université Aix-Marseille I - Provence (2006).
- [28] A. Y. Kupryazhkin, A. N. Zhiganov, D. V. Risovany, K. A. Nekrassov, V. D. Risovany, V. N. Golovanov, Simulation of diffusion of oxygen and uranium in uranium dioxide nanocrystals, *Journal of Nuclear Materials* 372 (2008) 233–238 (Jan. 2008).
- [29] Q. Bronchart, Développement de méthodes de champs de phase quantitatives et applications à la précipitation homogène dans les alliages binaires, PhD Thesis, Université de Cergy-Pointoise (2006).
- [30] L. A. Girifalco, R. J. Good, A theory for the estimation of surface and interfacial energies. I. Derivation and application to interfacial tension, *The Journal of Physical Chemistry* 61 (7) (1957) 904–909, tex.owner: rl211391 tex.timestamp: 2020.07.21 (1957).
- [31] IAEA (Ed.), *Thermophysical Properties of Materials for Nuclear Engineering: A Tutorial and Collection of Data*, IAEA, 2008 (2008).
- [32] V. Chalupecký, Numerical studies of Cahn-Hilliard equation and applications in image processing, in: *Proc. of Czech-Japanese Seminar in Appl. Math.*, 2004, pp. 4–7 (2004).
- [33] B. Sundman, U. R. Kattner, C. Sigli, M. Stratmann, R. Le Tellier, M. Palumbo, S. G. Fries, The OpenCalphad thermodynamic software interface, *Computational Materials Science* 125 (2016) 188–196 (2016).
- [34] Y. A. Coutinho, A. Kunwar, N. Moelans, Phase-field approach to simulate BCC-B2 phase separation in the Al₃CrFe₂Ni₂ medium-entropy alloy, *Journal of Materials Science* (Mar. 2022). doi:10.1007/s10853-022-07058-2.
URL <https://doi.org/10.1007/s10853-022-07058-2>